Spray Printing and Optimization of Anodes and Cathodes for High Performance Li-Ion Batteries

Sang Ho Lee*, Chun Huang, Colin Johnston and Patrick S. Grant

Department of Materials, University of Oxford, Oxford OX1 3PH, UK.

---

[*] Address correspondence to sangho.lee@materials.ox.ac.uk

ABSTRACT

A spray printing manufacturing approach to lithium-ion batteries was investigated with a focus on minimizing inactive fractions and maximizing energy and power densities of printable electrodes. Using a lithium titanate based anode initially and comparing with conventional electrodes, the effects of conductivity enhancer and binder fractions, post-calendaring effects, different electrode manufacturing methods, conductivity enhancer types and electrode thicknesses were explored, and optimum electrode structures were identified. These insights were then applied to a lithium iron phosphate based cathode, and full spray printed lithium titanate/lithium iron phosphate cell configurations were investigated. Notably, the full-cell battery with a 1:1 capacity ratio of lithium titanate to lithium iron phosphate had a stable specific energy density of ~ 300 Wh/kg and a power density of ~ 2500 W/kg, showing the promise of layer-by-layer spray printing to realize fully the intrinsic properties of electrode materials in lithium-ion battery cells.

KEYWORDS

Layer-by-layer structuring, spray printing, lithium titanate, lithium iron phosphate, lithium-ion battery.

1. Introduction

Driven by the need to reduce planet warming emissions from carbon-based fuels including coal, oil and natural gas, worldwide attention has increasingly focused on obtaining electrical energy from sustainable, environmentally-friendly power sources such as photovoltaics, wind turbines, hydropower and tidal energy. [1-4] In line with the technical progress on producing electricity, scientific effort is being expended in developing a range of complementary electrical energy storage technologies for electric vehicle and grid applications, with the ultimate aim to utilize electrical energy cost-effectively anytime and anywhere at the required scale, and with appropriate capacity and power characteristics.

Rechargeable Li-ion batteries that store and release electrical energy *via* the redox reaction of Li-ions shuttling between anodes and cathodes are the state-of-the-art for commercial electrochemical energy storage applications that take advantage of their high gravimetric and volumetric energy density (~ 260 Wh/kg and ~ 700 Wh/L, respectively), high cell voltage (~ 3.8 V) and still reducing cost. [5-7]

During the manufacture of the electrodes that are used in all Li-ion battery formats, the materials that form the electrode, including the electrochemically active materials, carbon-based conductivity enhancers and polymeric binders, are blended in an aqueous or non-aqueous media to form a homogeneous slurry or paste, and the resulting composite slurry is cast onto a metallic foil current collector using a doctor blade technique. [8-10] The success and quality of the final electrode structure is strongly dependent on the rheological properties of the composite slurry, determined by the binder fraction within the slurry, along with its wetting behavior, the electrode drying sequence, etc. The role of the binder is to provide robust adhesion of the electrode to the current collector and to provide mechanical coherence between the particulate electrode components within the electrode during repeated expansion and contraction of the active materials that usually accompany charge/discharge processes. However, the binder fraction should be minimized because it inhibits the electrochemical performance of the electrodes by blocking the residual inter-connected porosity essential for Li-ion movement throughout the electrode and by increasing resistance to electron transport between the materials within the electrode. Furthermore, excess use of inactive fractions (conductivity enhancers and binders) results in a decrease in both the gravimetric and volumetric energy density of the electrode and of the overall device. Therefore, there remains a demand for alternative electrode formulations and manufacturing approaches that provide the required long term electrode structural stability while allowing the intrinsic electrochemical properties of the active materials to be realized more fully, in both gravimetric and volumetric terms, i.e. the “parasitic” inactive mass and volume of the electrode should be minimized.

Printing technologies are used extensively in a wide range of processing and manufacturing areas, from simple typography to the manufacture of sophisticated biological tissues and organs, and have the potential advantages of simplicity, reproducibility, versatility, low cost and high throughput. [11-13] Amongst printing methodologies, spray printing produces structures or patterns based on the layer-by-layer deposition and drying of droplets of a suspension, and can be flexibly applied to a wide range of suspension chemistries and substrates. [14,15]

Spray printing has been suggested as an emerging technology that can substitute for conventional slurry casting for the manufacture of electrochemical energy storage electrodes when extra performance or functionality is required. [16] Guo *et al.* reported sprayed polymer scaffold frameworks for enhancing Si-based Li-ion battery performance; [17] Kim *et al.* and Singh *et al.* demonstrated all spray painted batteries, including anodes, cathodes and electrolyte; [18,19] Beneventi *et al.* demonstrated pilot-scale spray deposited electrodes; [20] and Wu *et al.* proposed flexible battery electrodes based on the spray approach. [21] In particular, our group has demonstrated and reported diverse, scalable electrode structures for supercapacitors as well as Li-ion batteries based on a spray printing route using various types of electrode materials including carbon nanotubes, carbon nanofibers, graphene, TiO_2, Fe_2O_3, Fe_3O_4, etc. [22-30] Recently, multi-layered electrode structures were shown to improve Li-ion diffusion and the volumetric capacity of Li-ion battery configurations based on the layer-by-layer spray deposition of two types of TiO_2 with porous and non-porous morphologies, [31] forming electrodes that are difficult to achieve using conventional battery electrode manufacturing technologies.

Here, we perform a systematic optimization of spray printed electrodes to establish the best structural arrangements and combinations of the constituent materials for a Li-ion battery system, i.e. we consider both anodes and cathodes and investigate full-cell performance based on optimized versions of both electrodes. Initially, the half-cell performance of a $Li_4Ti_5O_{12}$ (LTO) that offers stable capacity at ultra-fast charge/discharge conditions (e.g. 10 and 20 C) and during repeated charge/discharge cycles (> 500 cycles) because of its zero-strain property and no formation of a passivated solid electrolyte interphase [32,33] was studied. The aim was to understand the intrinsic behavior of spray printed electrodes according to systematic changes in selected parameters and to establish basic design rules that were then applied to cathodes and full-cells. Key parameters for electrode optimization were: (1) minimizing inactive fractions; (2) quantifying the effect of calendaring on the electrode performance; (3) exploring the comparative performance of identical spray printed and slurry cast electrodes; (4) optimizing the types and fraction of conductivity enhancers; and (5) investigating electrode thickness-dependent properties. Using the arising insights, a final optimization was conducted to boost full-cell battery performance based on an optimized, spray printed LTO-based anode and a spray printed $LiFePO_4$ (LFP)-based cathode, which showed a specific energy density of ~ 302 Wh/kg at 0.1 C and a power density of ~ 2420 W/kg at 10 C. The materials selected here are model systems to demonstrate optimization effects, for which comparative literature data is available, and are used to exemplify how new manufacturing approaches can extend the balance of power and capacity in known cell systems, and to suggest how the potential of future battery materials may be fully realized.

2. Experimental section

2.1. Materials

LTO particles of ~ 100 nm diameter and polymeric binders (carboxymethyl cellulose, CMC) were obtained from Sigma Aldrich, UK. LFP particles of ~ 3 μm diameter were obtained from Hydro-Québec, Canada. Conductivity enhancers (Super P, SP) were purchased from MTI Corporation, USA. Carbon nanotube (CNT) and graphene plate (GP) conductivity enhancers were obtained from Thomas Swan & Co. Ltd., UK.

2.2. Spray printing process

For the spray suspension, active materials, conductivity enhancers and binders in controlled weight fractions were suspended into a mixture of deionized (DI) water and isopropyl alcohol (IPA) in a DI:IPA volume ratio of 60:40 using sonication for 30 min, where DI water is required to dissolve the CMC binder, and IPA is required to disperse the particulates of LTO and carbon-based conductivity enhancers in the suspension. On the basis of the previous work, the suspension formulated with a DI:IPA volume ratio of 60:40 has optimum stability without any obvious sedimentation of the solid electrode constituents, providing the best deposition efficiency onto the current collector. [34] A current collector was fixed on a vacuum chuck of a hot plate that set to a temperature higher than the boiling point of the fugitive liquid mixture of DI water and IPA (e.g. > 100 °C). The liquid suspension was then sprayed at an atomizing air pressure of 0.4 bar onto this heated current collector in a well-ventilated fume cupboard. The spray nozzle moved in a pre-programmed pattern in the *x* and *y* plane at a fixed spray distance *z* for multiple cycles, leading to the layer-by-layer formation of an electrode over areas greater than 25 cm × 25 cm (but larger areas are easily available with a larger hot plate). The electrode thickness was controlled precisely by a combination of tuning the number of spray scan cycles and modifying the solid fraction in the suspension.

2.3. Electrochemical performance

Electrode electrochemical behavior was investigated using coin cells (CR2032), assembled from thoroughly dried electrodes in an Ar-filled glovebox (H_2O < 0.1 ppm, O_2 < 0.1 ppm). For half-cell batteries, pure Li chips (99.9% trace metals basis, MTI) were used as a counter/reference electrode. In the case of full-cells, the spray printed LTO-based anode electrodes, formulated with a 95:2:1:2 mass ratio of LTO:CNT:SP:CMC, were coupled with spray printed LFP cathodes, formulated with a 95:2:1:2 mass ratio of LFP:CNT:SP:CMC. The anode and cathode electrodes were electrically separated by a polyethylene separator (Cellgard 2400) soaked into 1 M $LiPF_6$ electrolyte solution in a 1:1 mixture (by volume) of ethylene carbonate and dimethyl carbonate (Merck). Galvanostatic charge/discharge tests for both half-cells and full-cells were conducted at room temperature using an Arbin battery cycler (Arbin BT-G-25). Electrochemical impedance spectroscopy (EIS) was performed in the range of 1 MHz to 100 mHz after the first three charge/discharge cycles (Gamry 6000). The charge/discharge capacities of the half-cell batteries were calculated according to the total electrode weight including LTO (or LFP), conductivity enhancers and binders. The theoretical capacity of LTO and LFP was assumed to be ~ 175 mAh/g. [35,36]

3. Results and Discussion

3.1. Manufacture

The layer-by-layer spray printing process is shown schematically in Fig. 1. The process comprises two stages: (1) preparation of liquid spray suspension, and then (2) spraying of the suspension through a spray nozzle onto the heated current collector, resulting in fast *in situ* drying of each layer as the electrode forms incrementally. For successful layer-by-layer structuring, it is critical that the spray suspension has sufficient rheological stability so that there is no setting of the solid content but is also sufficiently dilute (~ 5×10^{-3} g/mL), offering facile pumping from the suspension reservoir to the spray head and stable atomization (no pulsing). Successful layer-by-layer deposition involves the successive superimposition of suspension droplets on the heated current collector while ensuring there is no excessive liquid build-up or re-suspension of pre-formed layers.

3.2. Minimizing the inactive fraction

The Li-ion storage performance of the spray printed LTO-based electrodes was investigated as a function of the electrochemically inactive fraction, including SP and CMC, in four spray printed electrodes with controlled fractions of LTO, SP and CMC in the mass ratio: (1) 70:20:10, (2) 80:10:10, (3) 90:5:5 and (4) 95:3:2. Fig. 2a shows a scanning electron microscope (SEM) image of the surface of a typical spray printed LTO-based electrode. The contrived, concave surface arose from the fast drying of the bi-solvent carrier on the heated current collector. Fig. 2b displays a magnified view, showing the fine scale LTO and SP particles uniformly mixed with CMC binder. Fig. 2c-f shows cross-sections of the four spray printed LTO-based electrodes with different fractions of electrode components. The thickness of all electrodes was maintained constant at ~ 10 µm.

Fig. 3 shows the corresponding gravimetric rate capability for the four electrodes at charge/discharge rates of 0.1, 0.2, 0.5, 1, 2, 5, 10 and 20 C. As the LTO weight fraction increased from 70 to 95 wt% (and the inactive fractions decreased from 30 to 5 wt%), discharge capacity increased progressively at all rate conditions, noting that the electrode gravimetric capacities (Table 1) were calculated based on the total electrode weight including LTO, SP and CMC, which is more relevant for practical implementation than using the active weight alone. Similar to the gravimetric data, a trend of increasing electrode volumetric capacity with increasing LTO weight fraction is shown in Fig. S1, providing an insight that higher fractions of inactive constituents contribute only to parasitic mass. In the Nyquist plots in the inset of Fig. 3, the semi-circles in the high/medium frequency region indicated the charge transport resistance at the interface between electrodes and electrolyte, while the inclined lines in the low frequency domain represented the Warburg impedance corresponding to Li-ion diffusion behavior within the electrodes. [37,38] As the fraction of the conductivity enhancer (SP) increased, the diameter of the semi-circle reduced, indicating an improvement in electrode charge transport. The 95:3:2 electrode had a slightly smaller charge transport resistance than the 90:5:5 formulation, despite its lower fraction of conductivity enhancer, implying that using a lower fraction of the insulating CMC binder also contributed to improved electrode charge transport.

3.3. Calendaring

The effect of calendaring electrodes with a LTO:SP:CMC mass ratio of 95:3:2 was investigated, and SEM images in Fig. 4a and 4b show the electrode surface morphology before and after calendaring. The initially comparatively rough electrode (Fig. 4a) was markedly smoother after calendaring (Fig. 4b) and appeared more dense, apart from regions of the larger drying craters previously shown in Fig. 2a that persisted. The electrode thickness was reduced by ~ 20 % by calendaring (see the insets in Fig. 4a and 4b and Table 2) during which micron-scale porosity tended to be crushed and at least partially filled as material rearranged under the calendaring load.

Fig. 5 shows the discharge capacity profiles at increasing charge/discharge rate for spray printed LTO-based electrodes before and after calendaring. The electrodes had similar gravimetric discharge capacities at all rates, with only a slightly higher capacity of ~ 110 mAh/g at 20 C for the as-printed electrode when compared with ~ 103 mAh/g for the equivalent calendared electrode. The inset in Fig. 5 shows the volumetric discharge capacities obtained by normalizing the gravimetric capacities by the loading densities (g/cm^3), given in Table 2. Once normalized by total electrode volume, the discharge capacities were similar before and after calendaring, with only a slightly increased capacity for calendared electrodes in the range of 0.1 to 5 C, which was attributed to their reduced thickness (see Table 2). Overall, the as-printed electrodes had comparable gravimetric and volumetric rate performance regardless of the calendaring process, implying the possibility that the spray printing approach may simplify electrode manufacturing procedure. Hereafter, all spray printed electrodes are reported without calendaring unless otherwise stated.

3.4. Spray printing versus slurry casting

To investigate the potential benefits of the layer-by-layer spray printed electrodes, conventional slurry cast equivalent electrodes were prepared by a standard doctor blade process using slurries with a 95:3:2 mass ratio for LTO:SP:CMC. For the slurry cast electrodes, no calendaring was conducted for a fair comparison with the as-printed electrodes. At relatively low charge/discharge rates of 0.1 to 2 C, the spray printed and slurry cast electrodes had similar gravimetric discharge capacities, as shown in Fig. 6a, because differences in electrode structure had no effect on ion dynamics at these low C-rates. However, the gap between deliverable capacities and the influence of electrode structure became larger as the rate increased to 20 C, where the spray printed electrode (~ 110 mAh/g) had ~ 25 % higher capacity than the slurry cast equivalent (~ 90 mAh/g), as given in Table 3. As shown in Fig. 6b, the volumetric capacity for the spray printed electrode was also superior to the slurry cast electrode at 10 and 20 C.

The galvanostatic discharge capacity plots, cycled at a charge/discharge rate of 1 C as shown in Fig. 6c, further support the robust integrity of the spray printed electrode over the slurry casting equivalent: after 300 cycles, the spray printed electrode had a discharge capacity of ~ 130 mAh/g, indicating ~ 93 % retention of the 1st discharge capacity (~ 140 mAh/g), whereas the slurry cast electrode retained a capacity of ~ 120 mAh/g (~ 85 % of the 1st discharge capacity). The spray printed and slurry cast LTO-based electrodes had a coulombic efficiency of almost 100 % up to the 300th cycle (inset of Fig. 6c).

3.5. Conductivity enhancers

The effect of electrical conductivity enhancers was investigated using three materials: SP, CNTs and GPs, with the intention of exploring electrode performance as a function of the morphology of the electrical conductivity enhancers (e.g. 0-, 1- and 2-dimensional morphology, respectively). [39,40] Fig. 7a and 7c shows cross-sections of ~ 10 µm thick spray printed LTO-based electrodes with a controlled fraction of CNTs or GPs respectively. Fig. 7b and 7d is magnified images of each of the electrode cross-sections. The CNTs were shown to be well-dispersed and entangled with agglomerates of LTO and SP particles (Fig. 7b), while the GPs (likely consisting of several layers of graphene) were well-distributed amongst the other electrode materials (Fig. 7d).

To quantify an optimized fraction or combination of the conductivity enhancers, spray printed electrodes were prepared with controlled fractions of CNTs or GPs as described in Table S1 and S2. As shown in the bar graphs of Fig. 8a and 8d, as the CNT (or GP) fraction increased from 0 to 3 wt%, the SP fraction decreased correspondingly, from 3 to 0 wt%, so that the total conductivity fraction was fixed at 3 wt%. Fig. 8b shows the rate performance of spray printed LTO-based electrodes with a change in CNT fraction from 0 to 3 wt%. The electrode with only CNTs (3 wt%) showed a higher deliverable discharge capacity at 10 and 20 C than the electrode with only SP (3 wt%), which might be ascribed to the superior conductivity of CNTs. [41,42] However, the electrode with a mixture of 2 wt% CNT and 1 wt% SP had the highest deliverable capacity of ~ 125 mAh/g at 20 C of all combinations (see the magnified inset), which was further investigated using EIS, as shown in the series of Nyquist plots in Fig. 8c. Similar to the trend in the rate performance, the electrode with 2 wt% CNT and 1 wt% SP had the smallest charge transport resistance (~ 95 Ω). In Fig. 8e, as the GP fraction increased from 0 to 3 wt%, and the SP fraction decreased from 3 to 0 wt%, the electrode rate capability at 20 C increased progressively. The corresponding Nyquist plots in Fig. 8f again show reducing electrical resistance, from ~ 125 Ω to ~ 80 Ω with increasing the GP fraction, consistent with the rate capability data.

Fig. 9a and 9b exhibits the gravimetric and volumetric capacity retention profiles at different C-rates for electrodes with 3 wt% SP, with 3 wt% GP and with a mixture of 2 wt% CNT and 1 wt% SP. Here, the rate capacity retention is defined as the ratio of the discharge capacities obtained at 0.1, 0.2, 0.5, 1, 2, 5, 10 and 20 C to the discharge capacity at 0.1 C. It is inevitable that the rate capacity retention for all electrodes reduced with increasing C-rates, but the electrode with 2 wt% CNT and 1 wt% SP had the best retention (81 %) of gravimetric (Fig. 9a) and volumetric (Fig. 9b) capacity at 20 C when compared with the electrode with 3 wt% GP (78 %) and with 3 wt% SP (74 %). The galvanostatic discharge capacity profiles for these three electrodes, cycled at a constant charge/discharge rate of 1 C, are shown in Fig. 9c. All the electrodes sustained excellent capacity retention after 300 cycles. At the 300th cycle, the electrode with a mixture of 2 wt% CNT and 1 wt% SP delivered a discharge capacity of ~ 142 mAh/g (~ 97 % of the 1st discharge capacity), while the electrode with 3 wt% GP and with 3 wt% SP had a capacity of ~ 141 mAh/g (~ 96 % of the 1st discharge capacity) and ~ 132 mAh/g (~ 92 % of the 1st discharge capacity), respectively. Beyond the first few initial conditioning cycles, all the electrodes had a coulombic efficiency of almost 100 % up to the 300th cycle, as also shown in Fig. 9c.

3.6. Electrode thickness

The electrochemical properties of spray printed LTO-based electrodes with controlled thicknesses of 10, 20, 40 and 80 µm were investigated, as shown in the electrode cross-sections of Fig. 10a-d, and summarized in Table 4. Here, all the spray printed electrodes were formulated with the LTO:CNT:SP:CMC mass ratio of 95:2:1:2.

Fig. 11a shows the thickness-dependent rate performance at 0.1, 0.2, 0.5, 1, 2, 5, 10 and 20 C. At relatively low charge/discharge rates of 0.1 to 1 C, the electrodes had almost identical discharge capacities, but the difference in the deliverable capacity at high rates (≥ 5 C) became significant as the electrode thickness increased from 10 to 80 µm at 20 C. The 10 µm thick electrode delivered a discharge capacity of ~ 125 mAh/g, sustaining ~ 81 % of the discharge capacity at 0.1 C, whereas the 20 and 40 µm thick electrodes had a discharge capacity of ~ 120 mAh/g and ~ 80 mAh/g at 20 C, respectively, and eventually, the thickest 80 µm thick electrode had a capacity close to zero at 20 C. In terms of volumetric capacity (Fig. S2), this overall tendency was reproduced.

To investigate the thickness-dependent electrode reaction kinetics further, the Li-ion diffusion coefficient for the different thicknesses (Fig. 11b) was calculated from cyclic voltammetry (CV) measurements at scan rates between 0.1 and 20 mV/s, as presented in Fig. S3a-d. As the scan rate increased from 0.1 to 20 mV/s, the anodic current density peaks at approximately 1.75 V increased progressively. Fig. S3e-h shows plots of the anodic peak current density against the square root of the scan rate for the different electrode thicknesses. The peak current density was proportional to the square root of the scan rate, and the effective Li-ion diffusion coefficient within the electrode was estimated using the Randles-Sevcik equation: [43,44]

$$I_p = 0.4463n\ FAC_0(nF\upsilon D_{Li}/RT)^{1/2} \qquad (1)$$

where I_p is the peak current [A], n is the number of electrons transferred, F is the Faraday constant [C/mol], A is the electrode area [cm^2], C_0 is the molar concentration of the Li-ions in the electrode [mol/cm^3], D_{Li} is the Li-ion diffusion coefficient [cm^2/s], υ is the scan rate [V/s], R is the Gas constant [J/K·mol], and T is the temperature [K]. From the best-fit slope of a I_p-versus-$\upsilon^{1/2}$ plot, the 10, 20, 40 and 80 µm thick LTO-based electrodes had effective Li-ion diffusion coefficients of ~ 2.48×10^{-12}, ~ 2.16×10^{-12}, ~ 1.91×10^{-12} and ~ 1.12×10^{-12} cm^2/s, respectively, as given in Fig. 11b and Table 4, confirming that increasing electrode thickness led to a reduction in the effective Li-ion mobility.

The galvanostatic discharge capacity profiles at a constant charge/discharge rate of 1 C showed a similar tendency, as shown in Fig. 11c: while the 10 µm thick electrode sustained ~ 97 % of the 1st discharge capacity even after 300 cycles, the capacity retention of the 20, 40 and 80 µm thick electrodes at the 300th cycle reduced to ~ 87 %, ~ 44 % and ~ 21 %, respectively.

3.7. Full-cell performance

On the basis of the proceeding data, an optimized LTO-based negative electrode was formulated with the LTO:CNT:SP:CMC mass ratio of 95:2:1:2. Similarly, a spray printed LFP-based positive electrode was formulated with the LFP:CNT:SP:CMC mass ratio of 95:2:1:2 (see Fig. S4 and Table S3). Further optimization for a full-cell utilizing the spray printed negative and positive electrodes was then investigated by changing the LTO:LFP capacity ratio as follow: (i) 1:0.5, (ii) 1:1, (iii) 1:1.5, (iv) 1:2 and (v) 1:3 (see Table 5). Here, the optimized 10 μm thick LTO anode electrode was fixed, and the LFP electrode weights and the corresponding thicknesses were varied because full-cell performance is generally controlled by cathode performance. [45,46]

Fig. 12a shows the Ragone plots for the resulting full-cell batteries with different LTO:LFP capacity ratios at various charge/discharge rates of 0.1, 0.2, 0.5, 1, 2, 5 and 10 C, noting that the full-cell performance was evaluated by normalizing the weight of the LTO anodes including LTO, conductivity enhancers and binders. When the capacity ratio of the cathode to the anode was less than 1:1, full-cell batteries showed a relatively poor specific energy density of ~ 100 Wh/kg due to a deficiency of Li-ions from the cathode side. On the other hand, as the capacity ratio of the anode to the cathode increased from 1:1 to 1:3, the electrode energy density increased to ~ 300 Wh/kg at relatively low charge/discharge rates, and the electrodes had similar corresponding power densities at all rates, with only a slightly higher power of ~ 2420 mAh/g at 10 C for the 1:1 LTO:LFP capacity ratio. Difference in full-cell performance for the different LTO:LFP capacity ratios became more significant when the Ragone plot was re-estimated using the mass of the LFP cathode, as shown in the inset of Fig. 12a. With increasing the LTO/LFP capacity ratio, from 1:1 to 1:3, both the specific energy and power performances decreased drastically, where the performance of the 1:2 and 1:3 ratio was even lower than that of the 1:0.5 ratio. As expected, the full-cell battery with a balanced 1:1 LTO:LFP capacity ratio showed the best performance in terms of both specific energy and power density: a specific energy density of 302 Wh/kg at 0.1 C and a specific power density of 2420 W/kg at 10 C. LTO is generally considered to suffer little or no loss of Li-ions from solid electrolyte interphase formation, which is associated with its relatively high Li-ion insertion voltage of 1.55 V (*vs.* Li/Li^+), as shown in the CV data in Fig. S3a-d, [47,48] supporting the best full-cell performance at the 1:1 LTO:LFP capacity ratio.

Fig. 12b shows the charge/discharge plots at various rates for the spray printed full-cell with a 1:1 LTO:LFP capacity ratio, with a discharge capacity of ~ 153 mAh/g at 0.1 C, ~ 145 mAh/g at 1 C and ~ 120 mAh/g at 10 C, showing rate capabilities comparable with other LTO/LFP battery cells, as shown in Table S4, where many of the comparable data relied on metal doping or other techniques to boost capacity, or used high inactive fractions that were not taken into account in the gravimetric capacity data. Fig. 12c presents the galvanostatic discharge energy density as a function of cycle at a constant charge/discharge rate of 1 C for a full cell with a 1:1 LTO:LFP ratio, sustaining a superior energy density of ~ 245 Wh/kg after 500 cycles. The cell had a coulombic efficiency of almost 100 % up to the 500th cycle, as also shown in the inset of Fig. 12c. The photograph in Fig. 12c shows two fully spray printed cells with balanced 1:1 LTO:LFP capacity lighting up two red light-emitting diodes (LED) on a toy safety guard rail that is placed on an A5 (~ 20 cm × 15 cm) spray printed LTO-based electrode, indicating the easy practical implementation of layer-by-layer spray printed electrodes.

4. Conclusions

Li-ion battery electrodes based on LTO and LFP were fabricated using a layer-by-layer spray printing approach. Spray printed electrodes allowed a low fraction (≤ 5 wt%) of inactive components including conductivity enhancers and polymeric binders and thus promoted excellent gravimetric and volumetric capacities. The spray printed electrodes showed good electrode integrity during repeated lithiation/delithiation processes even at high charge/discharge rates (＞ 20 C), without the need for post-fabrication calendaring. The spray printed electrodes displayed a superior rate performance over conventional slurry cast equivalent electrodes in terms of both gravimetric and volumetric capacities at 10 and 20 C. Adding a small portion (2 wt%) of CNTs and reducing carbon black additions in both negative and positive electrodes showed a further benefit in high rate capability. As electrode thicknesses increased from 10 to 80 μm, both the gravimetric and volumetric capacity retention of spray printed electrodes at high C-rates (＞ 10 C) decreased due to a reduction in effective Li-ion mobility as there was less time available for Li-ion diffusion to reach all parts of the thicker electrodes. Full-cell spray printed batteries with a 1:1 LTO:LFP capacity ratio had a stable specific energy density of ~ 300 Wh/kg at 0.1 C and a specific power density of ~ 2420 W/kg at 10 C, without the need for metal doping or similar enhancements. Layer-by-layer spray printing offers a wide design space in terms of optimizing the non-active electrode content and allows different balances of power and energy density to be explored; it may also offer a generic and flexible platform to enable the next generation of electrochemical energy storage materials.

Acknowledgments

This work was supported by Innovate UK, grant number 102655, project ALICE - Advanced Lithium Ion Capacitors and Electrodes”.

Appendix A. Supplementary data

Supplementary data related to this article can be found at https://doi.org/.

References

[1] H. J. Kim, S. H. Lee, A. A. Upadhye, I. Ro, M. I. Tejedor-Tejedor, M. A.; Kim, W. B. Anderson, G. W. Huber, Plasmon-Enhanced Photoelectrochemical Water Splitting with Size-Controllable Gold Nanodot Arrays, ACS Nano 8 (2014) 10756-10765.

[2] B. Y. Xia, Y. Yan, X. Wang, X. W. D. Lou, Recent progress on graphene-based hybrid electrocatalysts, Mater. Horiz. 1 (2014) 379–399.

[3] S. H. Lee, Y. Noh, W. B. Kim, Convex and Concave Square Arrays of Vertical SnO_2 Nanowire Bundles toward Lithium-Ion Storage Electrodes, Energy Technol. 5 (2017) 1507-1513.

[4] P. G. Bruce, B. Scrosati, J. -M. Tarascon, Nanomaterials for Rechargeable Lithium Batteries, Angew. Chem. Int. Ed. 47 (2008) 2930–2946.

[5] S. H. Lee, Y. -R. Jo, Y. Noh, B. -J. Kim, W. B. Kim, Stripe- or Square-Patterned Arrays of Tin Dioxide Nanowires for Use in Lithium-Ion Battery Electrodes, J. Power Sources 367 (2017) 1-7.

[6] G. Gao, H. B. Wu, X. W. D. Lou, Citrate-Assisted Growth of $NiCo_2O_4$ Nanosheets on Reduced Graphene Oxide for Highly Reversible Lithium Storage, Adv. Energy Mater. 4 (2014) 1400422.

[7] J. H. Pikul, H. G. Zhang, J. Cho, P. V. Braun, W. P. King, High-Power Lithium Ion Microbatteries from Interdigitated Three-Dimensional Bicontinuous Nanoporous Electrodes, Nat. Commun. 4 (2013) 1732.

[8] X. Zhu, X. Yang, C. Lv, S. Guo, J. Li, Z. Zheng, H. Zhu, D. Yang, New Approach to Create TiO_2(B)/Carbon Core/Shell Nanotubes: Ideal Structure for Enhanced Lithium Ion Storage, ACS Appl. Mater. Interfaces 8 (2016) 18815-18821.

[9] H. Hu, L. Yu, X. Gao, Z. Lin, X. W. Lou, Hierarchical Tubular Structures Constructed from Ultrathin TiO_2(B) Nanosheets for Highly Reversible Lithium Storage, Energy Environ. Sci. 8 (2015) 1480-1483.

[10] Y. Ren, Z. Liu, F. Pourpoint, A. R. Armstrong, C. P. Grey, P. G. Bruce, Nanoparticulate TiO_2(B): An Anode for Lithium-Ion Batteries, Angew. Chem. Int. Ed. 51 (2012) 2164-2167.

[11] S. V. Murphy, A. Atala, 3D Bioprinting of Tissues and Organs, Nat. Biotechnol. 32 (2014) 773-785.

[12] S. H. Lee, B. Cho, S. Yoon, H. Jeong, S. Jon, G. Y. Jung, B. K. Cho, T. Lee, W. B. Kim, Printing of Sub-100-nm Metal Nanodot Arrays by Carbon Nanopost Stamps, ACS Nano 5 (2011) 5543-5551.

[13] Y. Xia, G. M. Whitesides, Soft Lithography, Angew. Chem. Int. Ed. 37 (1998) 550-575.

[14] G. -P. Rigas, M. M. Payne, J. E. Anthony, P. N. Horton, F. A. Castro, M. Shkunov, Spray Printing of Organic Semiconducting Single Crystals, Nat. Commun. 7 (2016) 13531.

[15] R. E. Sousa, C. M. Costa, S. Lanceros-Mendez, Advances and Future Challenges in Printed Batteries, ChemSusChem 8 (2015) 3539-3555.

[16] K. -H. Choi, D. B. Ahn, S. -Y. Lee, Current Status and Challenges in Printed Batteries: Toward Form Factor-Free, Monolithic Integrated Power Sources, ACS Energy Lett. 3 (2018) 220-236.

[17] J. Guo, C. Wang, A Polymer Scaffold Binder Structure for High Capacity Silicon Anode of Lithium-Ion Battery, Chem. Commun. 46 (2010) 1428-1430.

[18] N. Singh, C. Galande, A. Miranda, A. Mathkar, W. Gao, A. L. M. Reddy, A. Vlad, P. M. Ajayan, Paintable Battery, Sci. Rep. 2 (2012) 481.

[19] S. –H. Kim, K. –H. Choi, S. –J. Cho, J. T. Yoo, S. –S. Lee, S. –Y. Lee, Flexible/shape-versatile, bipolar all-solid-state lithium-ion batteries prepared by multistage printing, Energy Environ. Sci. 11 (2018) 321-330.

[20] D. Beneventi, D. Chaussy, D. Curtil, L. Zolin, E. Bruno, R. Bongiovanni, M. Destro, C. Gerbaldi, N. Penazzi, S. Tapin-Lingua, Pilot-scale elaboration of graphite/microfibrillated cellulose anodes for Li-ion batteries by spray deposition on a forming paper sheet, Chem. Eng. J. 243 (2014) 372-379.

[21] Y. Wu, H. Wu, S. Luo, K. Wang, F. Zhao, Y. Wei, P. Liu, K. Jiang, J. Wang, S. Fan, Entrapping Electrode Materials within Ultrathin Carbon Nanotube Network for Flexible Thin Film Lithium Ion Batteries, RSC Adv. 4 (2014) 20010-20016.

[22] X. Zhao, B. T. T. Chu, B. Ballesteros, W. Wang, C. Johnston, J. M. Sykes, P. S. Grant, Spray Deposition of Steam Treated and Functionalized Single-Walled and Multi-Walled Carbon Nanotube Films for Supercapacitors, Nanotechnology 20 (2009) 065605.

[23] B. Mendoza-Sánchez, B. Rasche, V. Nicolosi, P. S. Grant, Scaleable Ultra-Thin and High Power Density Graphene Electrochemical Capacitor

Electrodes Manufactured by Aqueous Exfoliation and Spray Deposition, Carbon 52 (2013) 337-346.

[24] C. Huang, N. Grobert, A. A. R. Watt, C. Johnston, A. Crossley, N. P. Young, P. S. Grant, Layer-by-Layer Spray Deposition and Unzipping of Single-Wall Carbon Nanotube-Based Thin Film Electrodes for Electrochemical Capacitors, Carbon 61 (2013) 525-536.

[25] C. Huang, P. S. Grant, One-Step Spray Processing of High Power All-Solid-State Supercapacitors, Sci. Rep. 3 (2013) 2393.

[26] C. Huang, N. P. Young, P. S. Grant, Spray Processing of TiO_2 Nanoparticle/Ionomer Coatings on Carbon Nanotube Scaffolds for Solid-State Supercapacitors, J. Mater. Chem. A 2 (2014) 11022-11028.

[27] C. Fu, P. S. Grant, Toward Low-Cost Grid Scale Energy Storage: Supercapacitors Based on Up-Cycled Industrial Mill Scale Waste, ACS Sustainable Chem. Eng. 3 (2015) 2831-2838.

[28] C. Fu, A. Mahadevegowda, P. S. Grant, Fe_3O_4/Carbon Nanofibres with Necklace Architecture for Enhanced Electrochemical Energy Storage, J. Mater. Chem. A 3 (2015) 14245-14253.

[29] C. Huang, J. Zhang, H. J. Snaith, P. S. Grant, Engineering the Membrane/Electrode Interface To Improve the Performance of Solid-State Supercapacitors, ACS Appl. Mater. Interfaces 8 (2016) 20756-20765.

[30] C. Fu, A. Mahadevegowda, P. S. Grant, Production of Hollow and Porous Fe_2O_3 from Industrial Mill Scale and Its Potential for Large-Scale Electrochemical Energy Storage Applications, J. Mater. Chem. A 4 (2016) 2597-2604.

[31] C. Huang, N. P. Young, J. Zhang, H. J. Snaith, P. S. Grant, A Two Layer Electrode Structure for Improved Li Ion Diffusion and Volumetric Capacity in Li Ion Batteries, Nano Energy 31 (2017) 377-385.

[32] P. Wang, G. Zhang, J. Cheng, Y. You, Y. –K. Li, C. Ding, J. –J. Gu, X. –S. Zheng, C. –F. Zhang, F. –F. Cao, Recent progress on graphene-based hybrid electrocatalysts. Facile Synthesis of Carbon-Coated Spinel $Li_4Ti_5O_{12}$/Rutile-TiO_2 Composites as an Improved Anode Material in Full Lithium-Ion Batteries with $LiFePO_4$@N-Doped Carbon Cathode, ACS Appl. Mater. Interfaces 9 (2017) 6138–6143.

[33] C. –C. Yang, H. –C. Hu, S. J. Lin, W. –C. Chien, Electrochemical Performance of V-Doped Spinel $Li_4Ti_5O_{12}$/C Composite Anode in Li-Half and $Li_4Ti_5O_{12}$/$LiFePO_4$-Full Cell, J. Power Sources 258 (2014) 424-433.

[34] S. H. Lee, A. Mahadevegowda, C. Huang, J. D. Evans, P. S. Grant, Spray Printing of Self-Assembled Porous Structures for High Power Battery Electrodes, J. Mater. Chem. A 6 (2018) 13133-13141.

[35] X. Sun, M. Hegde, Y. Zhang, M. He, L. Gu, Y. Wang, J. Shu, P. V. Radovanovic, B. Cui, Structure and Electrochemical Properties of Spinel $Li_4Ti_5O_{12}$ Nanocomposites as Anode for Lithium-Ion Battery, Int. J. Electrochem. Sci. 9 (2014) 1583-1596.

[36] L. –H. Hu, F. –Y. Wu, C. –T. Lin, A. N. Khlobystov, L. –J. Li, Graphene-Modified $LiFePO_4$ Cathode for Lithium Ion Battery Beyond Theoretical Capacity, Nat. Commun. 4 (2013) 1687.

[37] S. H. Lee, W. B. Kim, Fabrication of Hierarchically Branched SnO_2 Nanowires by Two-Step Deposition Method and Their Applications to Electrocatalyst Support and Li Ion Electrode, J. Power Sources 307 (2016) 38-44.

[38] S. H. Lee, Y. Noh, Y. -R. Jo, B. -J. Kim, W. B. Kim, Carbon-Encapsulated SnO_2 Core-Shell Nanowires Directly Grown on Reduced Graphene Oxide Sheets for High-Performance Li-Ion Battery Electrodes, Energy Technol. 6 (2018) 1255-1260.

[39] M. H. Al-Saleh, Electrical and Mechanical Properties of Graphene/Carbon Nanotube Hybrid Nanocomposites, Synth. Met. 209 (2015) 41-46.

[40] B. Marinho, M. Ghislandi, E. Tkalya, C. E. Koning, G. de With, Electrical Conductivity of Compacts of Graphene, Multi-Wall Carbon Nanotubes, Carbon Black, and Graphite Powder, Powder Technol. 221 (2012) 351-358.

[41] A. Lekawa-Raus, J. Patmore, L. Kurzepa, J. Bulmer, K. Koziol, Electrical Properties of Carbon Nanotube Based Fibers and Their Future Use in Electrical Wiring, Adv. Funct. Mater. 24 (2014) 3661-3682.

[42] E. Y. Li, N. Marzari, Improving the Electrical Conductivity of Carbon Nanotube Networks: A First-Principles Study, ACS Nano 5 (2011) 9726-9736.

[43] M. Fehse, E. Ventosa, Is TiO_2(B) the Future of Titanium-Based Battery Materials? ChemPlusChem 80 (2015) 785-795.

[44] C. K. Park, S. B. Park, H. C. Shin, W. I. Cho, H. Jang, Li Ion Diffusivity and Rate Performance of the LiFePO4 Modified by Cr Doping, Bull. Korean Chem. Soc. 32 (2011) 191-195.

[45] S. Choi, T. Bok, J. Ryu, J. -I. Lee, J. Chon, S. Park, Revisit of Metallothermic Reduction for Macroporous Si: Compromise between Capacity and Volume Expansion for Practical Li-Ion Battery, Nano Energy 12 (2015) 161-168.

[46] K. Eom, T. Joshi, A. Bordes, I. Do, T. F. Fuller, The Design of a Li-Ion Full Cell Battery Using a Nano Silicon and Nano Multi-Layer Graphene Composite Anode, J. Power Sources 249 (2014) 118-124.

[47] H. S. Bhatti, D. H. Anjum, S. Ullah, B. Ahmed, A. Habib, A. Karim, S. K. Hasanain, Electrochemical Characteristics and Li+ Ion Intercalation Kinetics of Dual-Phase $Li_4Ti_5O_{12}/Li_2TiO_3$ Composite in the Voltage Range 0−3 V, J. Phys. Chem. C 120 (2016) 9553-9561.

[48] X. Sun, P. V. Radovanovic, B. Cui, Advances in Spinel $Li_4Ti_5O_{12}$ Anode Materials for Lithium-Ion Batteries, New J. Chem. 39 (2015) 38-63.

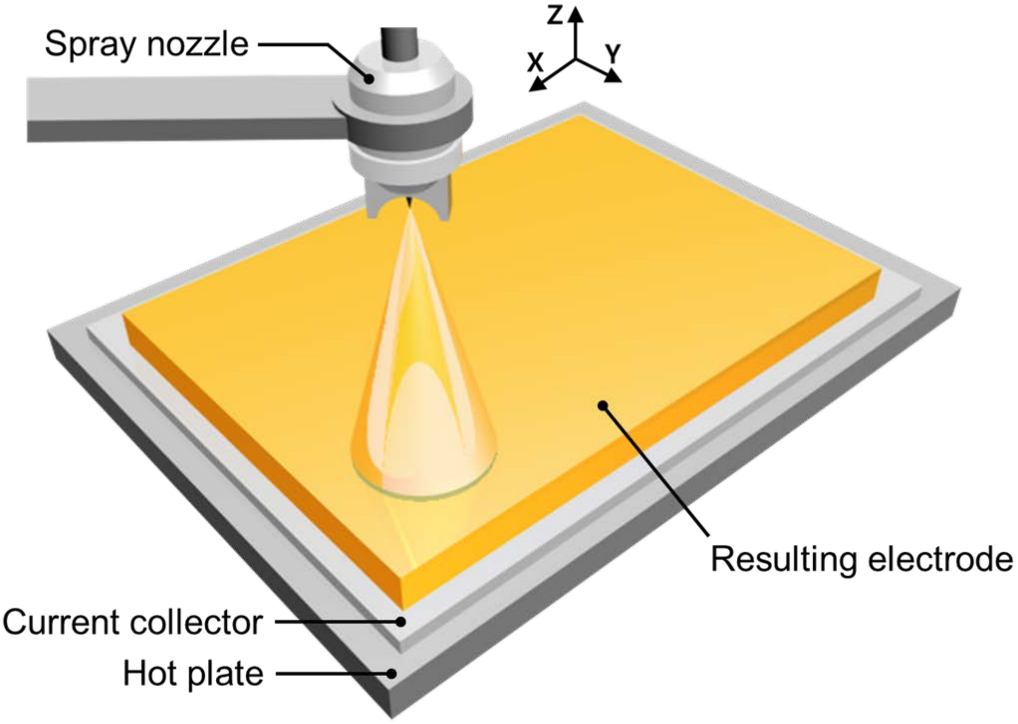

Fig. 1. The layer-by-layer formation of electrode structures onto a heated current collector based on the spray printing of suspension droplets atomized by a spray nozzle that moves in zig-zag pattern along *x* and *y* directions and offset distance *z* according to a pre-designed program.

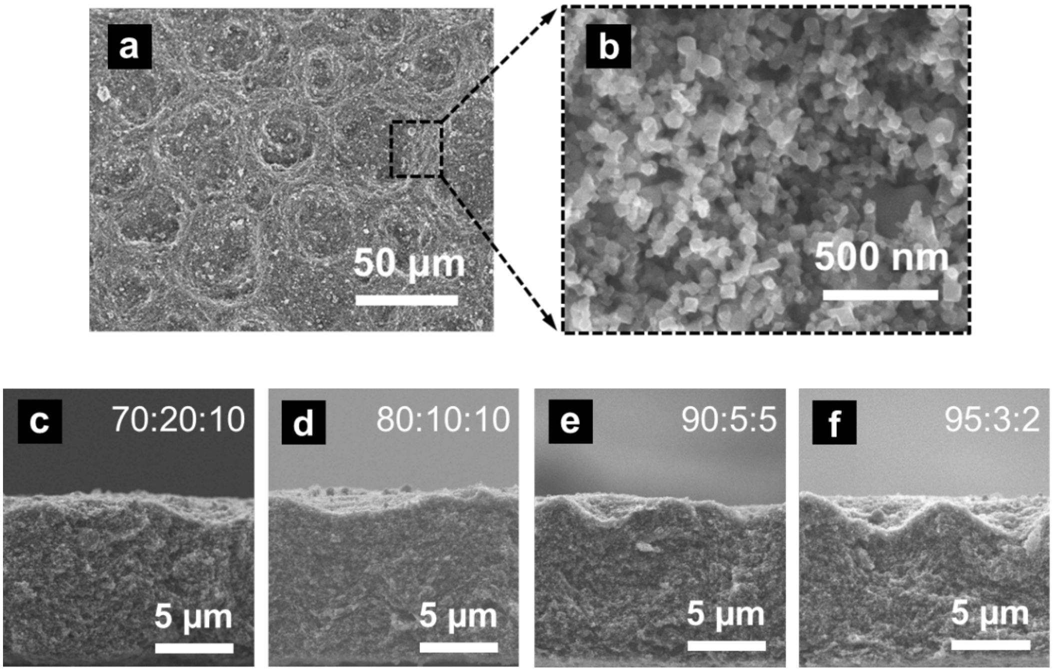

Fig. 2. SEM image of (a) the surface morphology of a ~ 10 μm thick spray printed LTO-based electrode. (b) The magnified surface of the spray printed electrode. Cross-sectional views of the ~ 10 μm thick spray printed electrodes with controlled fractions of LTO:SP:CMC in the mass ratio of (c) 70:20:10, (d) 80:10:10, (e) 90:5:5 and (f) 95:3:2.

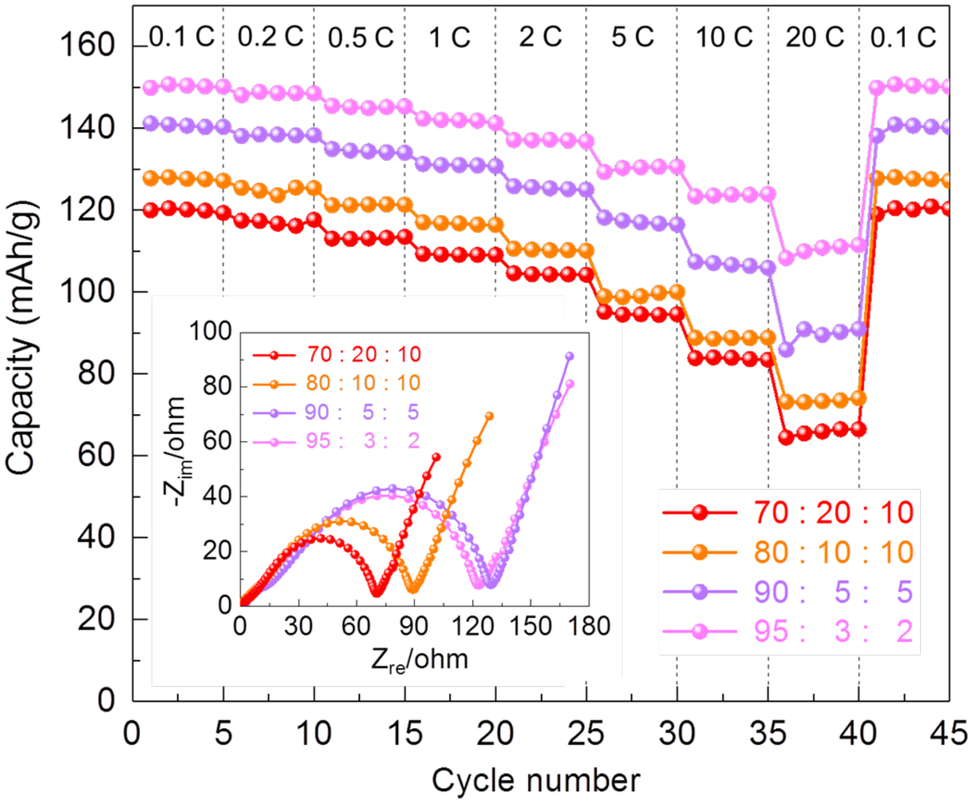

Fig. 3. Gravimetric discharge capacity plots with changes in the electrode LTO:SP:CMC fractions at various charge/discharge rates in the potential range of 1.0 to 2.5 V (*vs.* Li/Li$^+$). The inset shows the corresponding Nyquist plots.

Table 1. Summary of the spray printed LTO-based electrodes.

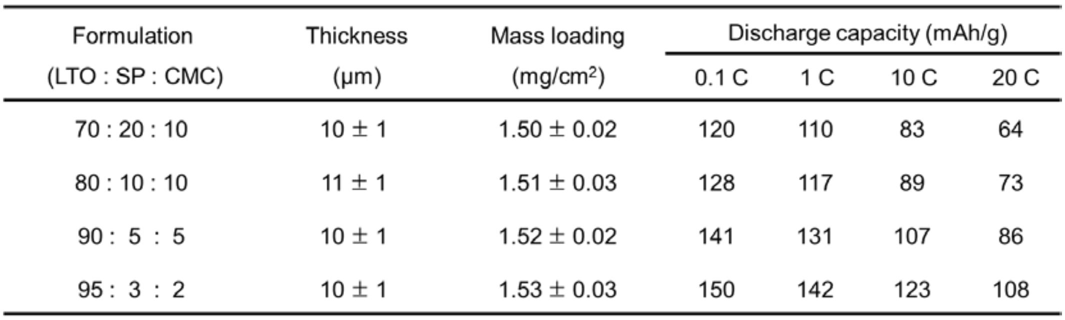

Formulation (LTO : SP : CMC)	Thickness (μm)	Mass loading (mg/cm^2)	Discharge capacity (mAh/g)			
			0.1 C	1 C	10 C	20 C
70 : 20 : 10	10 ± 1	1.50 ± 0.02	120	110	83	64
80 : 10 : 10	11 ± 1	1.51 ± 0.03	128	117	89	73
90 : 5 : 5	10 ± 1	1.52 ± 0.02	141	131	107	86
95 : 3 : 2	10 ± 1	1.53 ± 0.03	150	142	123	108

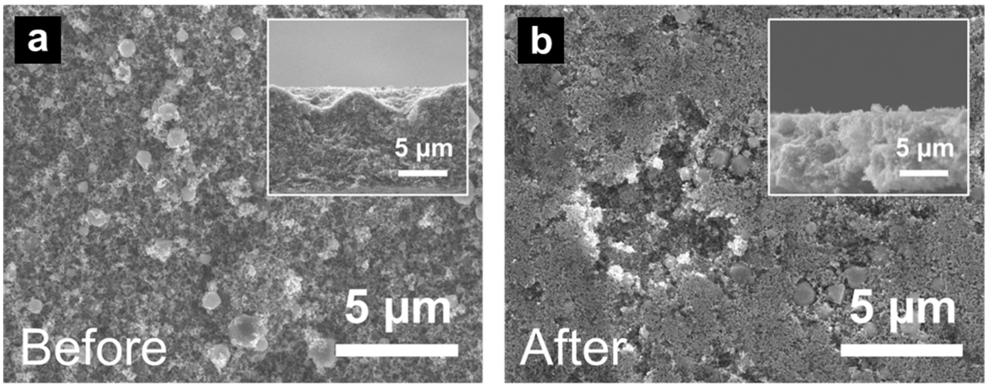

Fig. 4. SEM images of the spray printed LTO-based electrodes (a) before and (b) after calendaring. Each inset shows the corresponding electrode cross-section.

Table 2. Summary of LTO-based spray printed electrodes before and after calendaring.

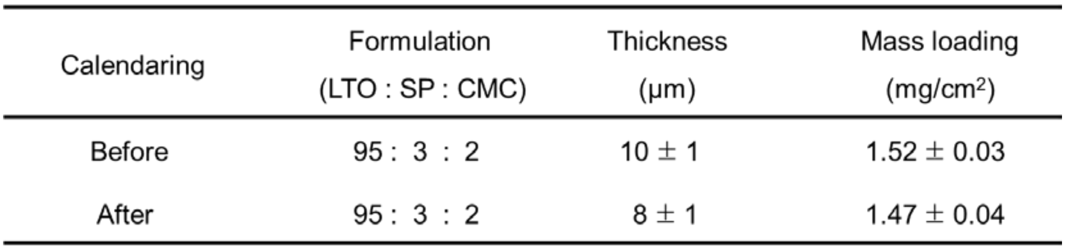

Calendaring	Formulation (LTO : SP : CMC)	Thickness (μm)	Mass loading (mg/cm^2)
Before	95 : 3 : 2	10 ± 1	1.52 ± 0.03
After	95 : 3 : 2	8 ± 1	1.47 ± 0.04

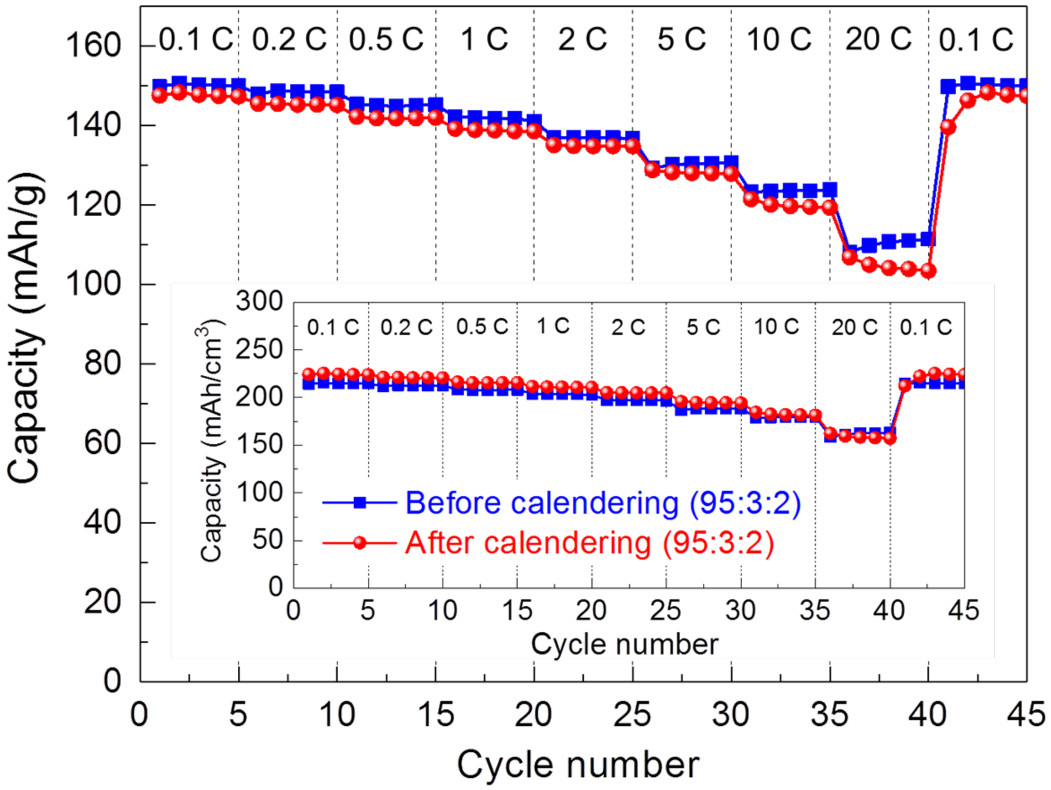

Fig. 5. Gravimetric discharge capacity plots of the LTO-based spray printed electrodes before and after calendaring at various charge/discharge rates in the potential range of 1.0 to 2.5 V (*vs.* Li/Li$^+$). The inset shows the corresponding volumetric discharge capacities for the electrodes before and after calendaring.

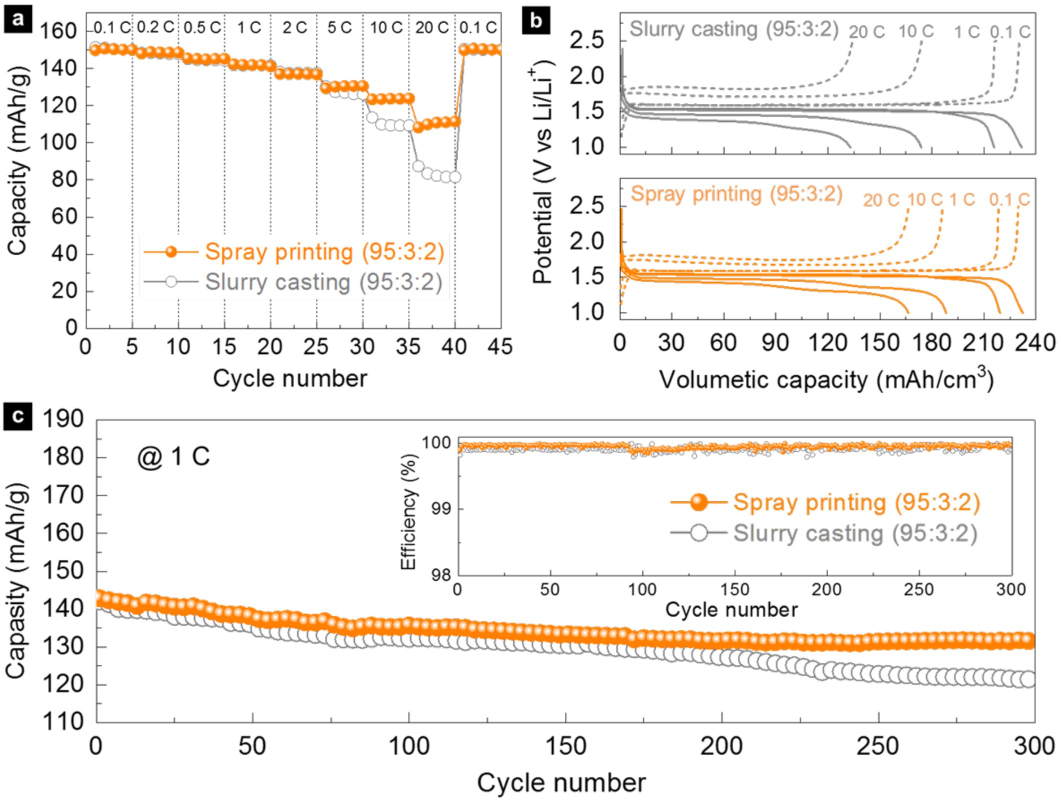

Fig. 6. (a) Gravimetric discharge capacity profiles of the LTO-based spray printed and slurry cast electrodes at various C-rates in the potential range of 1.0 to 2.5 V (*vs.* Li/Li$^+$). (b) Corresponding volumetric discharge capacity profiles for the two different types of electrodes. (c) Gravimetric discharge capacity profiles of the LTO-based spray printed and slurry cast electrodes at a constant charge/discharge rate of 1 C in the potential range of 1.0 to 2.5 V (*vs.* Li/Li$^+$) and the corresponding coulombic efficiency.

Table 3. Summary of spray printed and slurry cast LTO-based electrodes.

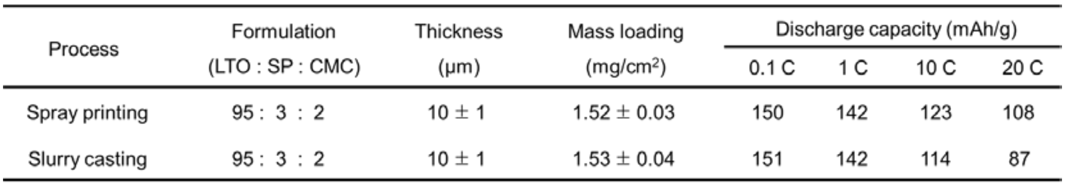

Process	Formulation (LTO : SP : CMC)	Thickness (μm)	Mass loading (mg/cm^2)	Discharge capacity (mAh/g)			
				0.1 C	1 C	10 C	20 C
Spray printing	95 : 3 : 2	10 ± 1	1.52 ± 0.03	150	142	123	108
Slurry casting	95 : 3 : 2	10 ± 1	1.53 ± 0.04	151	142	114	87

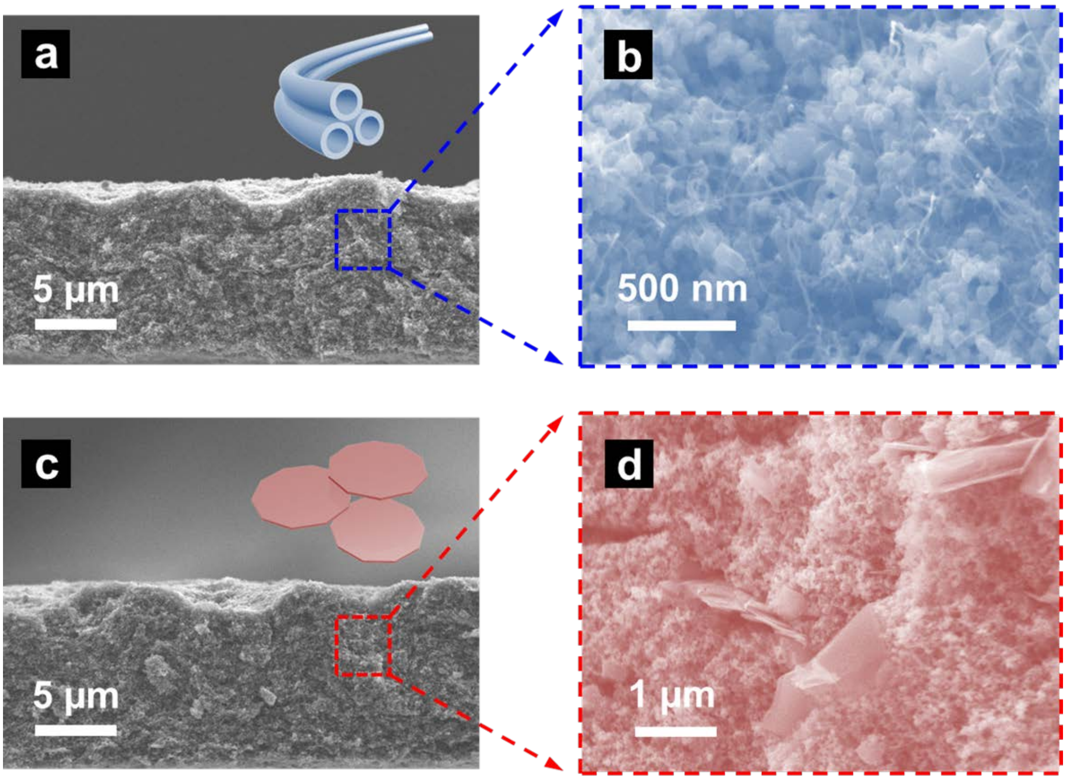

Fig. 7. (a) Cross-section of the spray printed LTO-based electrode with CNT conductivity enhancers. (b) Magnified SEM image of the electrode cross-section. (c) Cross-section of the electrode with GP conductivity enhancers. (d) Magnified electrode cross-section.

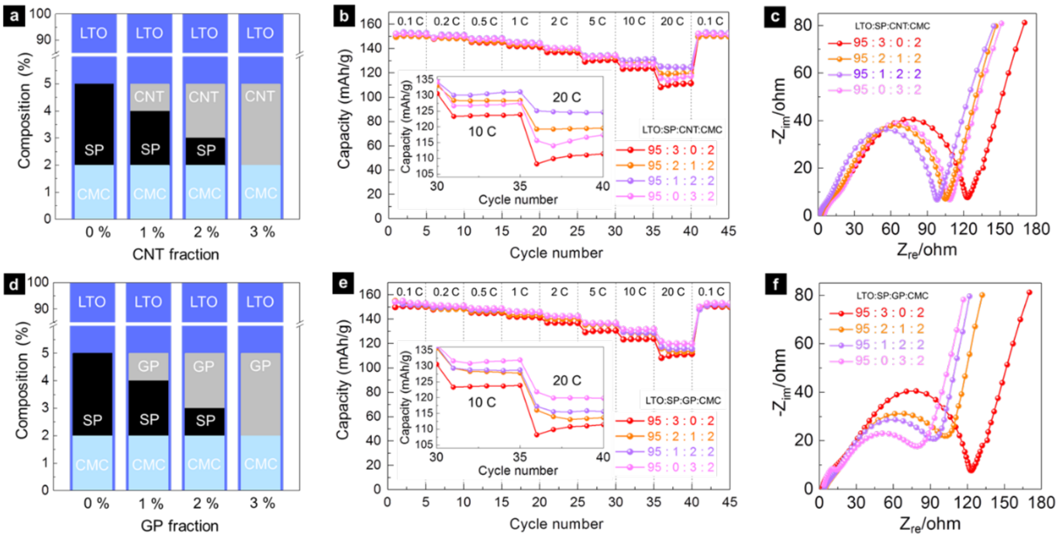

Fig. 8. (a) Summary of the CNT fraction in the spray printed LTO-based electrodes. (b) Discharge capacity plots of the spray printed LTO-based electrodes with controlled CNT fractions at various C-rates in the potential range of 1.0 to 2.5 V (*vs.* Li/Li$^+$). (c) Corresponding Nyquist plots for the electrodes. (d) Summary of the GP fraction in the spray printed electrodes. (e) Discharge capacity plots of the electrodes with controlled GP fractions in the potential range of 1.0 to 2.5 V (*vs.* Li/Li$^+$). (f) Nyquist plots for the electrodes.

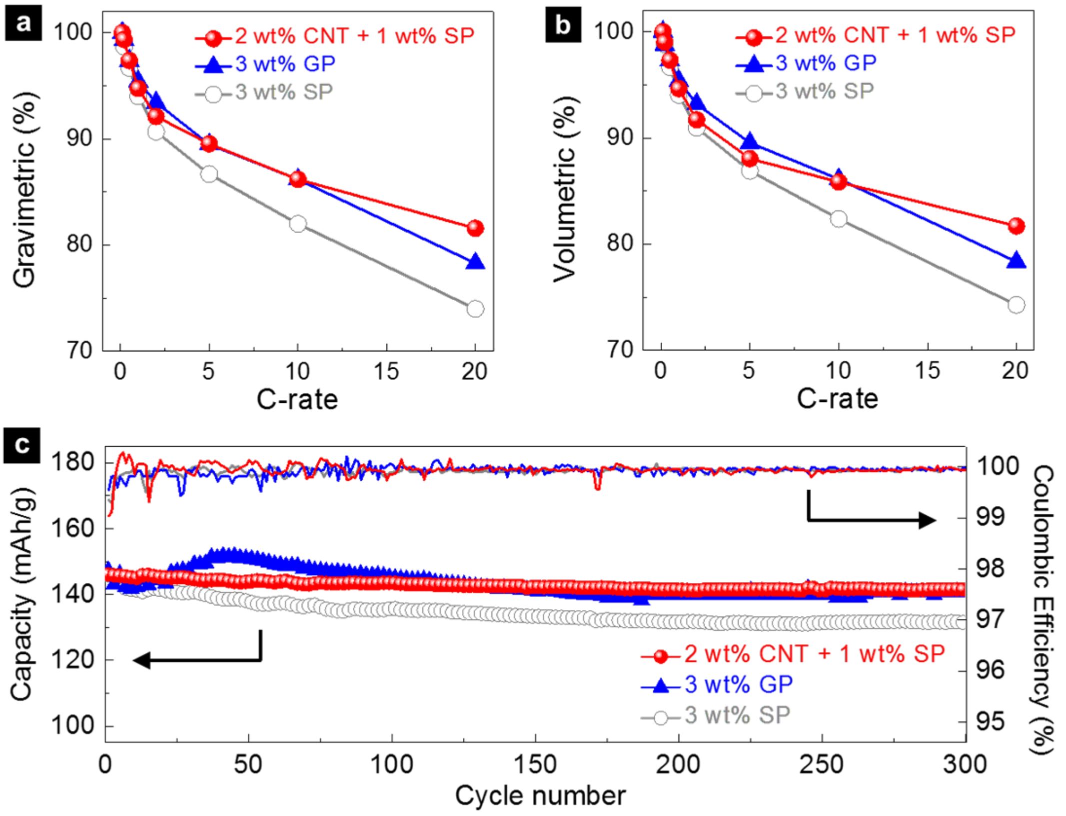

Fig. 9. (a) Gravimetric and (b) volumetric capacity retention profiles of the spray printed LTO-based electrodes with different conductivity enhancer fractions at various C-rates in the potential range of 1.0 to 2.5 V (*vs.* Li/Li$^+$). (c) Galvanostatic discharge capacity profiles of the electrodes with different conductivity enhancer fractions at 1 C in the potential range of 1.0 to 2.5 V (*vs.* Li/Li$^+$) and the corresponding coulombic efficiency.

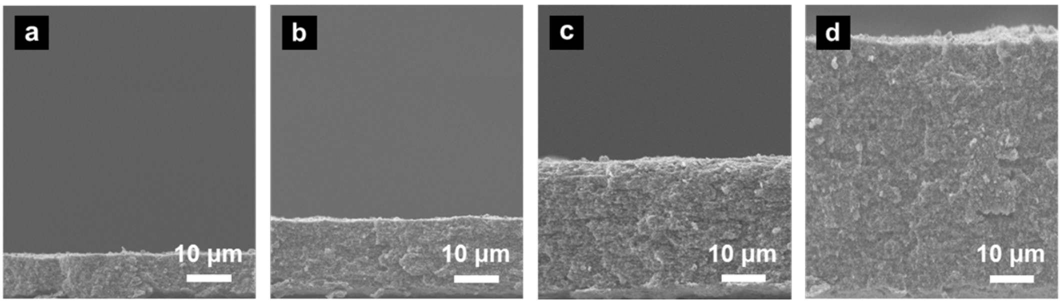

Fig. 10. Cross-sections of the LTO-based electrodes with controlled thickness of (a) 10 µm, (b) 20 µm, (c) 40 µm and (d) 80 µm.

Table 4. Summary of the spray printed LTO-based electrodes with varying thickness.

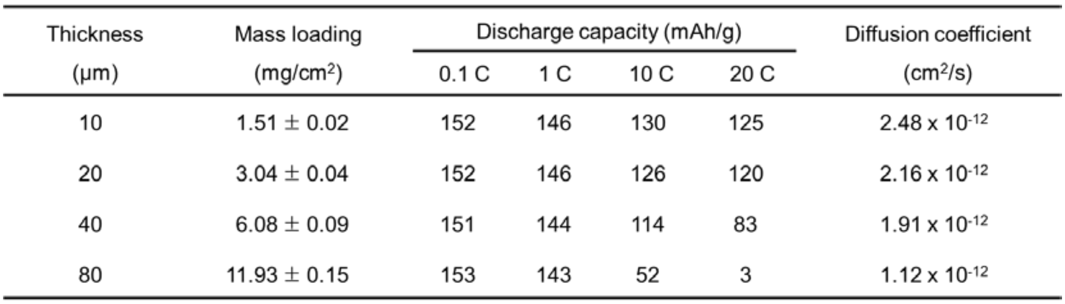

Thickness (μm)	Mass loading (mg/cm^2)	Discharge capacity (mAh/g)				Diffusion coefficient (cm^2/s)
		0.1 C	1 C	10 C	20 C	
10	1.51 ± 0.02	152	146	130	125	2.48×10^{-12}
20	3.04 ± 0.04	152	146	126	120	2.16×10^{-12}
40	6.08 ± 0.09	151	144	114	83	1.91×10^{-12}
80	11.93 ± 0.15	153	143	52	3	1.12×10^{-12}

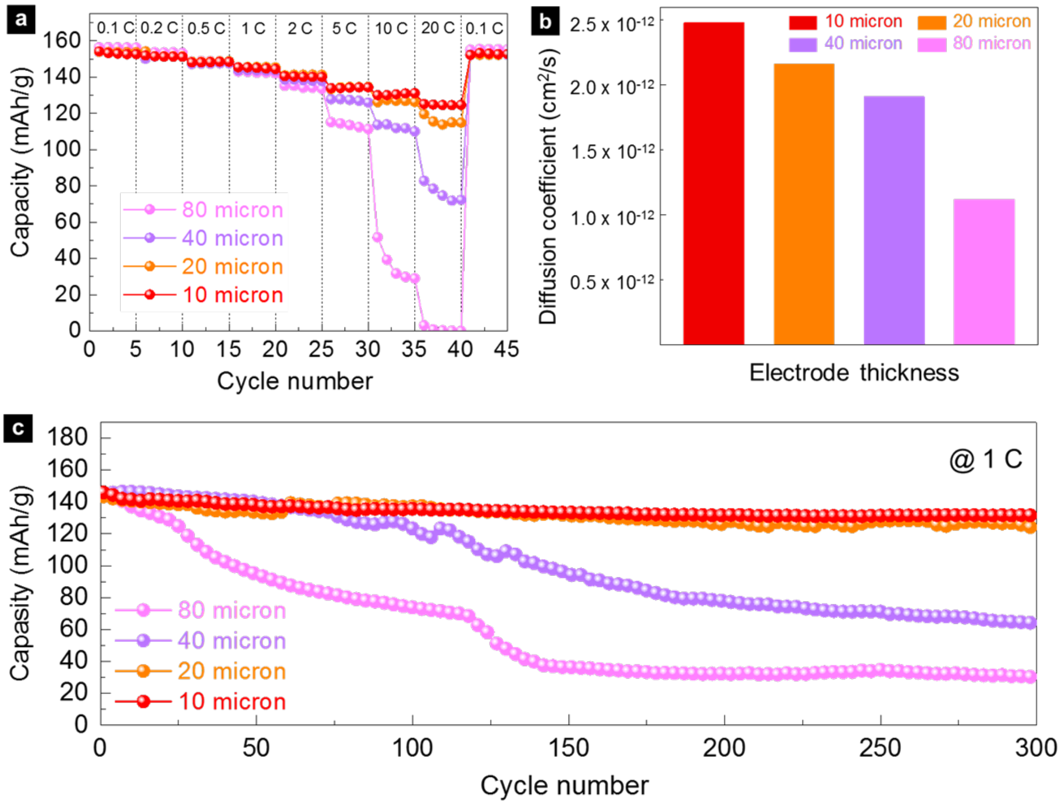

Fig. 11. (a) Gravimetric discharge capacity plots of the electrodes at various C-rates in the potential range of 1.0 to 2.5 V (*vs.* Li/Li$^+$). (b) Comparison of the thickness-dependent Li-ion diffusion coefficients. (c) Galvanostatic discharge capacity plots of the LTO-based electrodes with controlled thicknesses at 1 C in the potential range of 1.0 to 2.5 V (*vs.* Li/Li$^+$).

Table 5. Summary of the LTO-based anodes and the LFP-based cathodes.

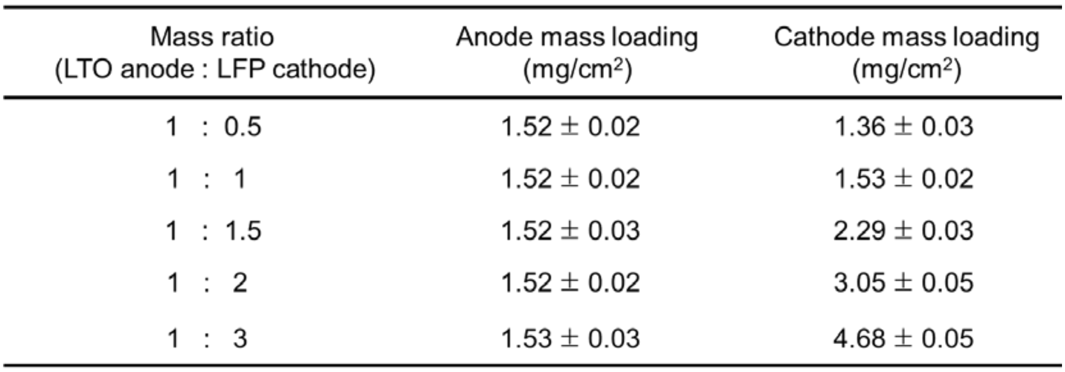

Mass ratio (LTO anode : LFP cathode)	Anode mass loading (mg/cm^2)	Cathode mass loading (mg/cm^2)
1 : 0.5	1.52 ± 0.02	1.36 ± 0.03
1 : 1	1.52 ± 0.02	1.53 ± 0.02
1 : 1.5	1.52 ± 0.03	2.29 ± 0.03
1 : 2	1.52 ± 0.02	3.05 ± 0.05
1 : 3	1.53 ± 0.03	4.68 ± 0.05

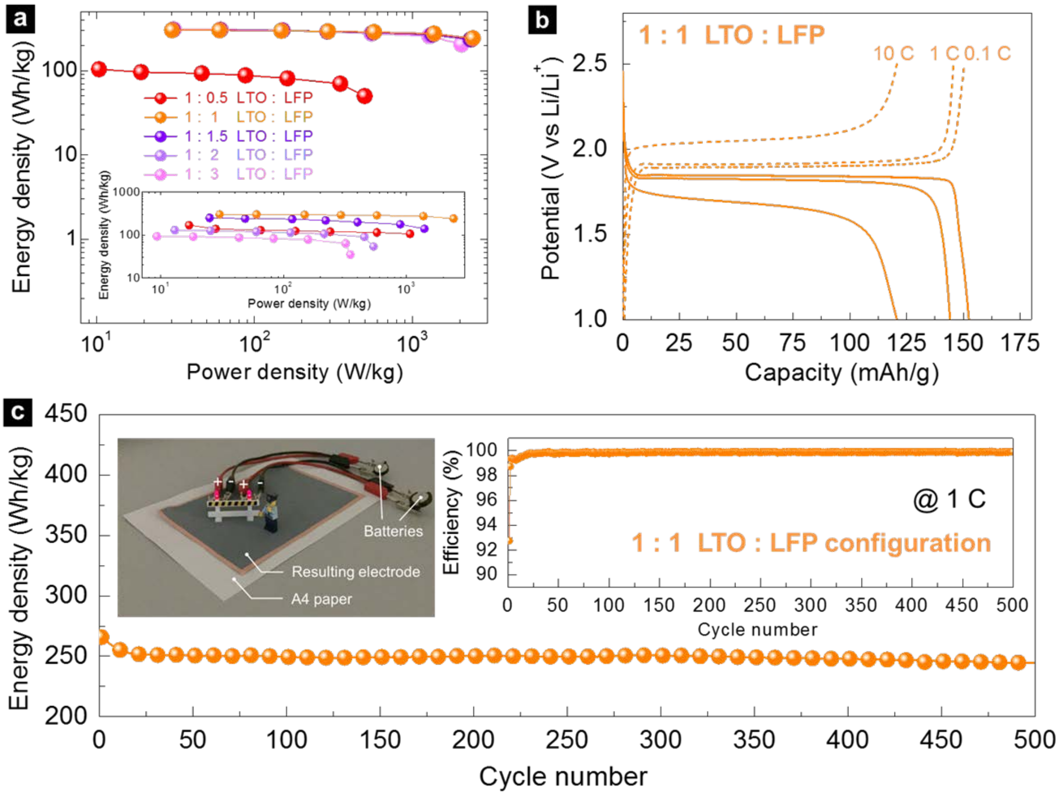

Fig. 12. (a) Ragone plot at various charge/discharge rates of 0.1, 0.2, 0.5, 1, 2, 5 and 10 C for the electrodes at various LTO:LFP capacity ratios. The inset provides the Ragone plot that was estimated on the basis of the mass of the LFP cathode including LFP, conductivity enhancers and binders. (b) Charge/discharge plots for the full-cell battery with a 1:1 LTO:LFP capacity ratio in the potential range of 1.0 to 2.5 V (*vs.* Li/Li$^+$). (c) Galvanostatic discharge energy density plots for the full-cell battery with a 1:1 LTO:LFP capacity ratio at 1 C in the potential range of 1.0 to 2.5 V (*vs.* Li/Li$^+$). The right-hand inset presents the coulombic efficiency of the electrode. Photograph showing two spray printed full-cell coin-type batteries with a 1:1 LTO:LFP capacity ratio connected to red LEDs that are placed on an A5-scale spray printed LTO-based electrode.

Electrochemical behavior of layer-by-layer spray printed electrodes was investigated based on lithium titanate anodes and lithium iron phosphate cathodes to quantify the best structural functionalities and combinations and then to establish basic design rules of printable electrode systems. The parameters investigated were: (1) minimizing inactive fractions; (2) quantifying the calendaring effect; (3) comparative performances of identical spray printed and slurry cast electrodes; (4) optimizing the conductivity enhancers; (5) investigating electrode thickness-dependent properties; and (6) balancing LTO:LFP capacities in full-cell battery systems.

Sang Ho Lee*, Chun Huang, Colin Johnston and Patrick S. Grant

Spray Printing and Optimization of Anodes and Cathodes for High Performance Li-Ion Batteries